Petrophysical properties of greensand as predicted from NMR measurements

Hossain, Zakir; Grattoni, Carlos A.; Solymar, Mikael; Fabricius, Ida Lykke

Published in:
Petroleum Geoscience

Link to article, DOI:
10.1144/1354-079309-038

Publication date:
2011

Petrophysical properties of greensand as predicted from NMR measurements

Zakir Hossain*[1], Carlos A. Grattoni[2], Mikael Solymar[3] and Ida L. Fabricius[1]

[1]Department of Environmental Engineering
Technical University of Denmark,
Miljøvej, Building 113, DK-2800 Lyngby, Denmark.
zaho@env.dtu.dk (Zakir Hossain), ilfa@env.dtu.dk (Ida L. Fabricius)

[2] Rock Deformation Research Ltd, School of Earth and Environment
University of Leeds, Leeds LS2 9JT, UK, c.a.grattoni@leeds.ac.uk

[3]Statoil ASA, Oslo, Norway, miso@StatoilHydro.com

*Corresponding author (e-mail: zaho@env.dtu.dk)

Number of words of text: 7634
Number of references: 36
Number of tables: 2
Number of figures: 13

Abstract

Nuclear magnetic resonance (NMR) is a useful tool in reservoir evaluation. The objective of this study is to predict petrophysical properties from NMR T_2 distributions. A series of laboratory experiments including core analysis, capillary pressure measurements, NMR T_2 measurements and image analysis were done on sixteen greensand samples from two formations in the Nini field of the North Sea. Hermod Formation is weakly cemented, whereas Ty Formation is characterized by microcrystalline quartz cement. The surface area measured by BET method and the NMR derived surface relaxivity are associated with the micro-porous glauconite grains. The effective specific surface area as calculated from Kozeny's equation and as derived from petrographic image analysis of Backscattered Electron Micrograph's (BSE), as well as the estimated effective surface relaxivity is associated with macro-pores. Permeability may be predicted from NMR by using Kozeny's equation when surface relaxivity is known. Capillary pressure drainage curves may be predicted from NMR T_2 distribution when pore size distribution within a sample is homogeneous.

Keywords: Greensand, glauconite, porosity, permeability, capillary pressure, NMR

Greensands are glauconite bearing sandstones composed of a mixture of stiff clastic quartz grains and soft glauconite grains. Glauconite grains are porous and composed of aggregates of iron-bearing smectitic or illitic clay. Porosity is thus found at two scales: macro-porosity between grains and micro-porosity within grains (Fig. 1). Greensand petroleum reservoirs occur world-wide, e.g. the mid-Cretaceous Safaniya Sandstone Member in Saudi Arabia (Cagatay *et al*. 1996), the Cretaceous Mardi Greensand in Australia (Hocking *et al*. 1988), the Lower Cretaceous Glauconitic sandstone in Alberta, Canada (Tilley & Longstaffe 1984), the Upper Cretaceous Shannon sandstone in Wyoming, USA (Ranganathan & Tye 1986), a lower Cretaceous Greensand offshore Ireland (Winn 1994) and a late Paleocene Greensand in central part of the North Sea (Slot-Petersen *et al*. 1998). However, evaluation of greensand reservoirs has challenged geologists, engineers and petrophysicsts. Glauconite has an effect on porosity, permeability and elastic properties of reservoir rocks (Diaz *et al*. 2003). Glauconite is also ductile (Ranganathan & Tye 1986) so it can cause non-elastic deformation of greensand (Hossain *et al*. 2009) and affect the reservoir quality. Greensands generally show low resistivity in the reservoir zone due to the large amount of bound water in the glauconite, yet free hydrocarbons can be produced because glauconite rather than being pore-filling is part of the sand grain framework (Slot-Petersen *et al*. 1998). Core analysis of greensand thus shows a poor relationship between porosity and permeability. Furthermore, greensand paramagnetic glauconite or pore filling berthierine may induce magnetic gradients on the pore level causing the NMR T_2 relaxation time to be shortened dramatically (Rueslåtten *et al*. 1998).

Nuclear Magnetic Resonance (NMR) is a non-invasive technique, and NMR measurements on reservoir core samples are done to obtain an improved interpretation of logging data. NMR measures the net magnetization of a hydrogen atom (^{1}H) in the presence of an external magnetic field. Hydrogen has a relatively large magnetic moment and is abundant in both water and hydrocarbons in the pore space of a sedimentary rock. NMR spectrometry involves a series of manipulations of the hydrogen protons found in fluids. A measurement sequence starts with proton alignment to a magnetic field followed by spin tipping, and decay. The quantities measured include signal amplitude which is proportional to the number of hydrogen nuclei and decay, also called relaxation time (Kenyon *et al*. 1995). Longitudinal relaxation time (T_1) measures the decay of spin alignment; transverse relaxation time (T_2) measures the decay of precession. Although T_1 measurements are more common in the literature, they are more time consuming than T_2 measurements. Hence, pulsed NMR logging tools preferentially measure T_2 for faster logging speeds (Straley *et al*. 1997). NMR transverse relaxation (T_2) of fluids confined in a porous rock is affected by pore surface, by the bulk relaxation process in the fluid and additionally by dephasing in case of molecular diffusion. T_2 may be expressed by the fundamental equation governing the NMR relaxation spectrum (Coates *et al*. 1999):

$$\frac{1}{T_2} = \frac{1}{T_{2Surface}} + \frac{1}{T_{2Bulk}} + \frac{1}{T_{2Diffusion}} \qquad (1)$$

Surface relaxation ($T_{2Surface}$) is the dominating mechanism in porous media, controlled by pore surface area. The relation between NMR relaxation and pore surface area results

from strong interaction between the protons and the surface because the surface relaxivity (ρ) causes rapid alignment of hydrogen protons on the pore wall, perhaps only a monolayer or two thick, while protons in the remaining fluid decay through itself (bulk relaxation), which is much slower (Howard *et al*. 1993). Bulk relaxation (T_{2Bulk}) is thus significantly smaller than the surface relaxation and so where relaxation of diffusion ($T_{2Diffusion}$) is slow, the relaxation ($\frac{1}{T_2}$) may be related to surface relaxivity and surface to volume ratio of pores (*Sp)*:

$$\frac{1}{T_2} = \rho_2 S_P \qquad (2)$$

NMR measurements provide information about the pore structure (*Sp*), the amount of fluid in-situ and interactions between the pore fluids and surface of pores. Thus, laboratory NMR measurements can be used to obtain porosity and correlate pore size distribution, clay bound water, and to estimate permeability and potentially predict capillary pressure curves from longitudinal relaxation time (T_1) and transverse relaxation time (T_2) distribution (Kenyon 1997). Numerous authors have explored the link between NMR measurements and petrophysical properties, e.g. the wettability investigation by NMR measurements by Al-Mahrooqi *et al*. (2003, 2006).

Porosity is one of the key parameter for hydrocarbon reservoir evaluation, and NMR is an effective tool to determine the porosity. However, several authors reported that there exist

106 significant differences between NMR porosity and core analysis porosity. Factors
107 influencing the T_2 measurements include paramagnetic minerals in the reservoir rock
108 which may cause $T_{2Diffusion}$ and hence reduce the T_2 relaxation time (Xie *et al*. 2008).
109 Aditionally, iron and other paramagnetic minerals affect the surface relaxivity and
110 produce a shift of the relaxation distribution to shorter times (Dodge *et al.* 1995).
111 Rueslåtten *et al.* (1998) studied NMR of iron-rich sandstone from the North Sea and
112 found a detrimental effect of iron bearing minerals on porosity estimation by NMR T_2.
113
114 Specific surface area is another significant petrophysical parameter for understanding the
115 physics of porous media and for permeability prediction. It was never fully integrated
116 into standard or special core analysis programs due to lack of petrophysical
117 understanding and concepts for correct evaluation (Riepe 1998). Nitrogen adsorption
118 methods (BET) yield high specific surface value as nitrogen enters the pores in the
119 sample. By using image analysis to determine the specific surface area, usually a much
120 smaller value is derived, and the value depends upon the resolution (Solymar *et al*. 2003).
121 The results of different methods reflect the different properties of pores at different
122 scales. By using a high resolution BET surface or a highly smoothed surface derived from
123 image analysis, the calculated permeability can be varied several orders of magnitude
124 (Riepe 1998). This is a concern because specific surface plays a vital role in
125 understanding and calibrating the T_2 spectra by estimating surface relaxivity (equation
126 (2)).
127

NMR relaxation is thus not only affected by the pore dimensions but also by the relaxivity of the rock surface. Quantitative knowledge of the surface relaxivity is needed when T_2 distributions are interpreted. Surface relaxivity is required in order to convert T_2 distribution into specific surface area, to calculate permeability and to convert T_2 time to capillary pressure curves. However, to measure surface relaxivity directly is not easy. Surface relaxivity may be estimated by scaling the normalized capillary pressure curve to the normalized T_2 distribution (Kleinberg 1996); or by comparing NMR T_2 distributions to specific surface area from nitrogen BET adsorption (Hidajat *et al*. 2002). Alternatively, it can be estimated by comparing NMR pore size distribution to pore size distribution from image analysis of thin sections (Howard *et al*. 1993; Kenyon 1997). Kleinberg (1996) concluded that the NMR effective specific surface area is closely associated with hydraulic radius of the sedimentary rock and calculated effective surface relaxivity from capillary pressure curves and T_2 distribution.

Permeability is a difficult property to determine from logging data, yet it is essential for reservoir characterization. Laboratory measurements provide absolute permeability at core scale which could be different from reservoir permeability. NMR is the only tool that attempts to estimate *in-situ* formation permeability (Hidajat *et al*. 2002; Glover *et al*. 2006). One of the most popular NMR derived permeability correlations is the Timur-Coates formula (Coates *et al*. 1999), and is implemented as:

$$k_{NMR} = (C\phi)^m \left(\frac{FFI}{BFI}\right)^n \quad (3)$$

where, ϕ is the porosity, *FFI* is the free fluid volume and *BFI* is the bound irreducible fluid, as determined from NMR measurements. Formation dependent constants *C*, *m* and *n* may be assumed to be 10, 4 and 2 for sandstones respectively, where NMR permeability, k_{NMR} is given in mD. However, this equation is simply an empirical derived relationship that links various NMR-derived parameters to permeability. Especially for diagenetically altered consolidated reservoir rocks, the complicated internal pore structures may not be described by this model, causing unrealistic permeability estimates, unless empirically calibrated parameters are used, which have no general physical meaning and thus are only valid for special facies types and for local investigations. Timur-Coates formula also indicates that porosity or pore volume strongly controls the permeability together with the effective specific surface area as expressed by $\frac{FFI}{BFI}$ in accordance with the equation of Kozeny (1927). For homogeneous sediments like chalk, the effective specific surface is equivalent to the one measured by nitrogen adsorption (BET) and Kozeny's equation works well without introducing empirical factors (Mortensen *et al*. 1998). However, for less homogenous sediments, like greensand, we can calculate an effective surface area (*Sp(Kozeny)*) from permeability and porosity by using Kozeny's equation. We infer that it is this effective surface that controls permeability.

Capillary pressure (P_c) curves can be determined only from core analysis, but NMR derived P_c curves provide a fast, cheap and non-destructive estimation. However, up to now, most authors have focused on the relation between T_2 distribution and P_c curves (Kleinberg 1996; Grattoni *et al*. 2003; Marschall *et al*. 1995; Volokitin *et al*. 1999) and the general conclusion is that, if the bulk relaxation and diffusion effects are ignored, a simple relationship between P_c and T_2 becomes:

$$P_c = \frac{K}{T_2} \qquad (4)$$

where, K is an empirical scaling factor introduced to predict capillary pressure curves. However, several authors, e.g. Kleinberg (1996) concluded that the match between capillary pressure and NMR relaxation curves are not universal. The simple relationship (equation (4)) reflects that both the T_2 distribution and P_c curves are affected by pore structures but overlooks the difference between the physics of the processes. Kewan & Ning (2008) discussed that in a pore and throat model of the pore space, the capillary pressure is sensitive to the pore throat, whereas the NMR measures the pore body size. Thus, the technique gives same information only when there is a constant ratio between them.

The combination of conventional core analysis, such as Helium porosity, Gas permeability, specific surface area by BET and image analysis of thin sections micrographs is proven to be very effective in the evaluation of normal reservoir rocks.

However, for glauconite bearing greensand where a high proportion of micro-porosity in glauconite grains creates an uncertainty with respect to fluid distribution and fluid saturation, an accurate determination of petrophysical properties by using conventional core analysis is difficult (Rueslåtten *et al*. 1998). The objective of this study is to predict petrophysical properties from NMR T_2 distributions which can be applied to *in-situ* well logging. Estimates of porosity, permeability, irreducible water saturation derived from NMR measurement were corrected with measurements from core analysis. The porosity obtained by using the different methods was compared for the greensand samples. The potential use of surface area data is also described and illustrated. Kozeny's equation was used for NMR permeability prediction and P_c curves were estimated from NMR measurements.

Geological setting of Nini Field

The Nini field is located in Siri Canyon which is part of a larger system of submarine canyons in the Paleocene in the Norwegian-Danish Basin running in an E-W to NE-SW direction towards the Central Graben (Fig. 2) (Stokkendal *et al*. 2009). The Nini accumulation is defined by a combined structural and stratigraphic trap, the anticlinal structure being induced through salt tectonics. The reservoir consists of sands deposited in the Siri Fairway (Schiøler *et al*. 2007).

The glauconite bearing sandstone in the Nini field was recognized by stratigraphic work in Statoil in the mid-1990s (Schiøler *et al*. 2007). It is formally included in the Hermod

Formation and in the older Ty Formation. These Paleocene reservoir sands are characterized by glauconite rich (20-30 vol %) fine grained, well sorted sand, embedded in hemiplegic to pelagic mud- and marl-stones, in which both quartz grains and glauconite pellets are part of the load-bearing matrix. The greensand beds thus occur in a shale-sequence. In the Nini wells, the Hermod sand was found to be more massive, more porous and more permeable than Ty sand (Fig. 3).

Method

We studied sixteen one and half inch horizontal core plugs from the two greensand formations of the Nini-1 well (7 samples from Hermod Formation and 9 samples from Ty Formation). The samples had already been used for routine core analysis and were chosen so as to cover the range of variation in porosity (25%-40%) and air permeability (60 mD-1000 mD). All cores were cleaned from brine and hydrocarbons by soxhlet extraction with methanol and toluene prior to analysis. Thin sections were prepared from the end of each plug and material from the end trimmings were used for X-ray diffraction (XRD) and BET analysis.

Routine core analysis

Helium porosity (ϕ_H) of the samples was measured by the gas expansion method. Helium porosity is a good measure of total porosity, including porosity in clay minerals, as no pores are so small that Helium cannot enter. Buoyancy of the cores in brine (Archimedes)

238 was also used to determine bulk volume on a fully saturated sample and pore volume was
239 calculated from grain density as measured by the gas expansion method. Complete
240 saturation was verified by comparing porosity measured by Helium expansion and by
241 Archimedes method. As porosity data from the two methods are within experimental
242 error, all samples were assumed to be fully brine saturated.
243
244 Klinkenberg corrected permeability was derived from permeability at a series of nitrogen
245 gas pressures. Specific surface area of the grain (S_g) was measured by BET method by
246 using nitrogen gas adsorption. Specific surface of pores from BET method (*Sp(BET)*) was
247 calculated by dividing S_g by porous fraction, (ϕ_H) and multiplying by grain fraction, (1-ϕ_H)
248 as:

249 $$Sp(BET) = S_g\left(\frac{1-\phi_H}{\phi_H}\right)\rho_g \qquad (5)$$

250
251 where, ρ_g is grain density.
252 The effective bulk specific surface (S) was obtained from Klinkenberg permeability (k)
253 and macro-porosity (ϕ) by using Kozeny's equation (Kozeny 1927) as:
254

255 $$k = c\frac{\phi^3}{S^2} \qquad (6)$$

256
257 where, c is Kozeny's factor which can be estimated from porosity via a simple model of
258 linear 3D interpenetrating tubes (Mortensen *et al.* 1998):
259

$$c = \left[4\cos\left\{ \frac{1}{3}\arccos\left(\phi \frac{8^2}{\pi^2} - 1 \right) + \frac{4}{3}\pi \right\} + 4 \right]^{-1} \quad (7)$$

According to equation (7), c increases from 0.15 to 0.25 as porosity increases from 0.05 to 0.5. Specific surface of pores from Kozeny's equation (*Sp(Kozeny)*) can then be calculated:

$$Sp(Kozeny) = \frac{S}{\phi} \quad (8)$$

$\frac{1}{Sp(Kozeny)}$ is equivalent to hydraulic radius and thus should be related to capillary pressure and T_2 relaxation, so we base the remaining analysis on *Sp(Kozeny)*.

Capillary pressure

The capillary pressure may be expressed by the fundamental equation:

$$P_c = \frac{2\sigma \cos\theta}{r_c} \quad (9)$$

where, r_c is the radius of pore throat, σ is the surface tension and θ is the contact angle. For water-wet conditions $\cos\theta$ becomes one, and in terms of specific surface of pore (*Sp*) equation (9) may be rewritten as:

$$P_c = S_P \sigma \quad (10)$$

279 Air brine drainage capillary pressure measurements were done on brine saturated
280 greensand samples by using the porous plate method at room temperature. Initially each
281 sample was saturated with simulated formation brine. The brine has a density of 1.06
282 g/cm^3 and a viscosity of 1.054 cP. Irreducible water saturation (S_{wi}) including clay
283 bound water was determined from capillary pressure curves and macro-porosity was
284 calculated as porosity above irreducible water saturation (Fig. 4b).
285
286
287
288

289 **Image analysis**

290

291 Polished thin sections were prepared from all samples in a plane perpendicular to the
292 flow direction during core analysis. A Philips XL40 Scanning Electron Microscope was
293 used for acquisition of Back Scattered Electron (BSE) images. The images are 1024 x
294 1024 byte greyscale images with a pixel length of 1.78 µm. This magnification resolves
295 the intergranular macro-porosity and leaves the micro-porosity unresolved. Each image
296 was filtered to remove the noise and thresholded to create a binary image prior to
297 analysis. Porosity determined in the images is called image porosity (ϕ_{image}). The image
298 analysis procedure is sensitive to porosity threshold, so image porosity was determined when
299 they are equal to macro-porosity determined from P_C measurements. The macro-porosity
300 determined by image analysis is within a narrow range (±2.5 p.u.) obtained by image analysis

along. The specific surface area or strictly speaking the specific perimeter (*S(image)*) of the solid grains was determined by using the method of Borre *et al*. (1995). According to Underwood (1970) and Solymar & Fabricius (1999) the specific perimeter (*S(image)*) may be approximated to the 3-D specific surface (*S)* by:

$$S = \frac{4}{\pi} S(image) \qquad (11)$$

Image specific surface of pores (S_p *(image)*) is thus calculated by using equation (8) where porosity is defined as macro-porosity determined from capillary pressure measurements.

NMR measurements

For NMR measurements all samples were saturated with brine (7.6 % NaCl). Complete saturation was verified by using the dry weight, the saturated weight, grain volume by Helium expansion, and brine density. All samples attained full brine saturation. All the measurements were performed with the samples sleeved in PTFE heat shrink as several were poorly consolidated. The weights and volumes of the heat shrink material were accounted for in the measurements.

The laboratory NMR measurements were performed using a Resonance Instruments MARAN 2 spectrometer at ambient pressure and 34^{o}C at a proton resonance frequency of 2.2 MHz. T_2 relaxations was measured using Carr-Purcel-Meiboom-Gill (CPMG) pulse

sequence. The T_2 relaxation curves were measured by using a Recycle Delay (Repetition Time) of 10 sec, Number of Echos 8000, CPMG inter echo spacing (τ) 200 μs and 100 scans. The $\pi/2$ and π pulses were 14.8μs and 29.6μs, respectively.

NMR porosity of the fully saturated samples was determined by using the total signal amplitude of each sample (by summing the amplitudes of the T2 distribution) and known standard of similar diameter. In this case the reference standard was a sealed glass vial, containing $3cm^3$ of 50,000 ppm NaCl and $17cm^3$ of deuterium oxide. Deuterium oxide does not have an NMR signal therefore this reference standard has an equivalent porosity of 15%. The same number of scans was used for the reference and the sample. NMR porosity is then calculated using the, total signal amplitude, the bulk volume, hydrogen index of both plug and reference and the equivalent porosity of the reference.

For determining the macro-porosity and micro-porosity we need a cutoff value from the T_2 distribution. For two samples (one from Hermod and one from Ty), the T_2 cutoff was determined in the laboratory by obtaining the T_2 distribution at two saturations, fully brine saturated and at irreducible water saturation as determined from capillary pressure curves. The analysis of the air-water systems is relatively easy as there is no NMR response from the air and the relaxation time is exclusively due to the protons in the water. The cutoff time is defined as the relaxation time at the point where the cumulative porosity of the fully saturated sample equals the irreducible water saturation (Fig. 4a). As the T_2 cutoff is determined from capillary pressure equilibrium experiments includes capillary bound fluid and trapped in micro-pores. A single T_2 cutoff value for each

formation was used for all samples of that formation. The cumulative porosity over the range $T_2 > T_{2cutoff}$ was the macro-porosity and below the range $T_2 < T_{2cutoff}$ was the micro-porosity or irreducible water saturation.

The NMR permeability model used in this work was obtained by combining equation (2), (6), and (8):

$$k = c\phi(T_2\rho_2)^2 \qquad (12)$$

In a similar way the capillary pressure NMR model was obtained combining equation (2) and (10):

$$P_c = \frac{\sigma}{\rho_2 T_2} \qquad (13)$$

The assumption of this model is that: 1- the pore structure controlling the T2 distribution and capillary pressure is a bundle of capillary tubes and the drainage is controlled by the hierarchy of pore sizes; 2- the surface relaxivity is constant overall the sample; 3- diffusion relaxation is negligible.

Results

The Helium porosity of greensand ranges from 28 to 42 p.u. (porosity units) with a maximum uncertainty 1.5 p.u. (Table 1). Klinkenberg corrected permeability ranges from

60 to 940 mD (Table 2). Permeabilities of Hermod samples are larger than Ty samples and correlates with porosity, whereas Ty data are more scattered (Fig. 5).

Petrographic thin section analysis indicates that the studied Paleocene greensands are well to very well sorted, dominated by grains of quartz but also large volumes of glauconite (20-25 vol %) (Fig. 6). Samples from Hermod Formation contain glauconite grains of size between 100 and 200 µm, some glauconite grains are larger (300 to 400 µm) (Fig. 1a). Samples from Ty Formation contain glauconite grains of size between 100 and 150 µm, although some glauconite grains are larger (200 to 300 µm) (Fig. 1b). The grains are subangular to sub-rounded for the both Formations. Hermod Formation is only weakly cemented, whereas samples from Ty formation contain cement of berthierine or microcrystalline quartz cement resulting in relative in a low permeability (Table 2). In both formations XRD analyses of separated glauconite grains show the presence of some expanding layers in the predominantly illitic glauconite.

The capillary pressure was obtained assuming 72 mN/m for the brine surface tension. Capillary pressure curves show that for the higher permeability Hermod Formation samples, the P_c curves are shifted toward low irreducible water saturation, whereas P_c curves for the lower permeability Ty Formation samples are shifted toward high irreducible water saturation (Figs 7a, c). Irreducible water saturation from capillary pressure was obtained at P_c 100 psi, and varied between 25% and 42% of the total porosity (Table 2).

The NMR T_2 distributions are presented in graphical form for each sample and the population is expressed in porosity units in Figures 7b, d. All T_2 distributions are bimodal. Each T_2 time corresponds to a particular pore size. If the rock has a single pore size then instead of a broader distribution there will be a single vertical line. Thus broader distributions reflect greater variability in pore size. We have determined a time cutoff of 5.21 ms for the sample 1-4 from Hermod Formation and 3.68 ms for sample 1A-141 from the Ty Formation. The short relaxation time component in a T_2 distribution of a rock is attributed to the water in glauconite. For the present greensand samples a peak close to 1 ms should correspond to glauconite water, whereas all samples also present a second peak close to 100 ms that corresponds to movable fluid. Higher permeability Hermod Formation samples show larger amplitude in the movable fluid than samples from Ty Formation; whereas lower permeability bearing Ty Formation sample show slightly larger amplitude in capillary bound and glauconite water (Figs 7b, d).

Discussion

Porosity

Helium porosity, Archimedes porosity and NMR porosity are compared in Figure 8. Helium porosity is associated with the total porosity of the sample including micro-porosity in glauconitic and it shows the highest values among the three types of porosity data. However, Archimedes and NMR porosity should also in principle represent the total porosity of a sample, but could be lower if water saturation is below 100%. Although the

412 Archimedes porosity is close to Helium porosity, NMR porosity tends to be lower. Both
413 macro-porosity and micro-porosity are underestimated by the NMR measurements (Figs
414 8c, d). The discrepancy between Archimedes porosity and NMR porosity could be due to
415 several factors. First, NMR and Archimedes porosity depend on saturation condition of
416 the sample. So we cannot rule out that during NMR measurement the saturation condition
417 was lower than that at the Archimedes measurements. Second, paramagnetic iron-bearing
418 minerals in reservoir rock may be an important factor influencing T_2 measurements as
419 shown by Dodge *et al.* (1995). The presence of paramagnetic ions increases the rate of
420 relaxation of the hydrogen proton. This is expected for greensand because glauconite and
421 berthierine are iron-bearing. These clay minerals have large surface area and high
422 magnetic susceptibilities leading to large internal gradients and short T_2 (Straley *et al*.
423 1997). Rueslåtten *et al.* (1998) illustrated the influence of chlorite (berthierine) and
424 glauconite on the difference between Helium porosity and NMR T_2 derived porosity
425 (delta porosity) and found broad positive correlation between delta porosity and chlorite
426 content, whereas they found no correlation with glauconite content. Thus they pointed to
427 the detrimental effect of chlorite or berthierine on porosity estimated by NMR. However,
428 we found only a vague negative correlation between delta porosity and bulk mineral
429 composition (glauconite, clay coating and pores filling) (Fig. 8b).
430

431 **Specific surface area**
432
433 Specific surface area with respect to pore (*Sp*), determined by three methods are
434 compared in Figure 10a. We found a large difference between the specific surface areas

435 as measured by BET method (*Sp(BET)*, 76-141 μm^{-1}) and calculated by Kozeny's
436 equation (*Sp(Kozeny)*, 0.27-0.95 μm^{-1}) and determined by image analysis (*Sp(image)*,
437 0.32-0.46 μm^{-1}). Nitrogen adsorption has a very high resolution; therefore this method
438 determines the specific surface of the total porosity, including micro-porosity. Based on
439 the Kozeny's equation, we estimated *Sp(Kozeny)* by using permeability determined on
440 the cores and macro-porosity. *Sp* by image analysis depends on the resolution of the
441 image (Solymar *et al*. 2003). However, *Sp* from image analysis at the present pixel size
442 and *Sp* from Kozeny's equation are in same order of magnitude which tells us that
443 resolution of image is sufficient and pixel size is small enough to determine *Sp* by image
444 analysis. The specific surface area of separated glauconite grains are in order of 1300-
445 1600 μm^{-1}, whereas the specific surface area of quartz grains is less than 1 μm^{-1}. So
446 rather than quartz grains, specific surface of glauconite grains are measured by BET
447 method. Thus, *Sp* by BET method is mainly reflected by the micro-pores of glauconite
448 grains and pore filling/lining clays, whereas *Sp* from Kozeny's equation and image
449 analysis is associated with effective surface and related to macro-porosity. We found that
450 *Sp* measured by BET method is well correlated with fraction of glauconite plus pore
451 filling clay minerals (Fig. 9c).
452
453 We found that irreducible water saturation ranges from 22% to 41% from capillary
454 pressure measurements and from 23% to 36% from NMR measurements. Considering
455 errors association with these two methods, irreducible water saturations are close to each
456 other. The high value of irreducible water saturation is due to the high specific surface of
457 glauconite. The micro-pores of glauconite remain brine filled even at a capillary pressure

458 of 100 psi. We found a positive correlation between irreducible water saturation
459 determined from P_c and NMR with *Sp* determined from BET method (Figs 9a, b). In
460 addition Figures 9a, b also show the tendency for low surface area samples to approach
461 minimum irreducible water saturation and for high surface area samples to remain more
462 saturated. A relationship between specific surface and irreducible water saturation has
463 been noted by several authors e. g. Hamada *et al*. (2001) where authors reported an
464 excellent correlation (R^2=0.98) between irreducible water saturation and specific surface
465 of pores.
466

467 **Surface relaxivity**

468

469 We compare four ways of estimating surface relaxivity in Figure 10b. Equation (2) shows
470 that surface relaxivity for NMR T_2 distribution is related to specific surface of pores.
471 Thus in absence of laboratory data, surface relaxivity may be evaluated by comparing T_2
472 distributions with *Sp(BET)*, *Sp(Kozeny)* or *Sp(image)*. This results in relaxivity value
473 ranges in order of 2.7-4.2 µm/s from *Sp(BET)*, 7-58 µm/s from *Sp(Kozeny)*, and 10-35
474 µm/s from *Sp(image)*. As an alternative, we used P_c curves and found that a surface
475 relaxivity of 20.4 µm/s for Hermod and of 28.4 µm/s for Ty Formation are needed to
476 generate Pc curves from NMR measurements. The surface relaxivity estimated based on
477 *Sp(BET)* would be controlled by micro-porosity in glauconite. We found an average
478 surface relaxivity by *Sp(BET*) of 3.42 µm/s, which is close to the 3.3 µm/s for glauconite
479 reported by Matteson et al. (1996). Surface relaxivity estimated from *Sp(Kozeny)* and

480 *Sp(image)* also should be effective surface relaxivity as it was calculated from effective
481 specific surface area.
482

483 **Permeability**

484

485 Kozeny's equation (equation (12)) was used to predict permeability from NMR T_2
486 distributions. Before applying this equation we highlight the similarities and differences
487 within T_2 distribution among samples (Fig. 11). The T_2 distribution of sample 1-18 peaks
488 at longer time than for sample 1-6, thus the larger porosity of sample 1-18 is due to the
489 larger pores which also cause higher permeability (Fig. 11a). The comparison of three
490 samples with similar distributions at shorter times is shown in Figure 11b. When the
491 larger peak (around 100 ms) becomes smaller and is shifted to larger times due to a small
492 number of intermediate pores, there is a small increase of the number of larger pores.
493 Thus, for these samples the permeability is not high although porosity is higher. We thus
494 cannot use average T_2 time or final T_2 time in equation (12) for permeability calculation.
495 So we modified the equation (12) by summing the total permeability among the T_2
496 distribution and only including the macro-porosity. Thus resulting:

497

498 $$k = c\phi\rho_2^2 \sum_{i=1}^{N} f_i (T_{2i})^2 \qquad (14)$$

499

where, *fi* is a fraction of the total amplitude of each T_{2i}. Kozeny factor c was calculated using equation (7).

The predicted permeability distribution obtained by using equation (14) is shown in Figures 11c, d. Below cutoff time, the amplitude of permeability is zero which means micro-porosity does not contribute to fluid flow. From cutoff time to 100 ms, the amplitude of permeability is small but above 100 ms the contribution of permeability increases.

Predicted permeability and measured permeability are compared in Figure12a by using surface relaxivity from *Sp(Kozeny)* (Average surface relaxivity for each depth interval), in Figure 12b by using surface relaxivity from *Sp*(image), in Figure 12c by using surface relaxivity from equation (13), and in Figure12d by using surface relaxivity from *Sp(BET)*. Predicted permeability is close to 1:1 line of measured permeability for case 1 and 2. The estimated permeability from Timur-Coates model is illustrated in Figure 12e. Predicted permeability using this model works rather well if we use C=8.3 which was optimized in a least-squares sense such that the sum of the squared error between the measured and predicted permeability is minimized. Predicted permeability from image analysis and measured permeability are compared in Figure 12f. Image permeability and NMR predicted permeability by using surface relaxivity from *Sp*(image) are equal.

Capillary pressure curves

We applied the value of surface relaxivity of 20.3 μm/s and 28.4 μm/s for Hermod Formation and Ty Formation sample respectively to generate the capillary pressure curves directly from the T_2 distribution by using equation 13 (Fig. 13). Capillary pressure curves overlay each other for low permeability samples. However, we found deviation between the P_c NMR and P_c lab for the high permeability sample from Hermod Formation. A deviation is to be expected, because we assumed uniform surface relaxivity within a sample and ignored diffusion relaxation. The calculated surface relaxivity is shown in Figure 13e for a sample from Hermod Formation and in Figure 13f for a sample from Ty Formation. A good match between P_c curves from laboratory and NMR measurement is found when average surface relaxivity is equal to surface relaxivity applied to predict P_c curves from NMR. In contrast, we found deviation between P_c curves from laboratory and NMR measurements when average surface relaxivity is not equal to the surface relaxivity need to match Pc curves. This variation of surface relaxivity within the sample is probably due to the large pores and higher permeability in the greensands of Hermod Formation.

Conclusion

The objective of this study is to predict petrophysical properties from NMR T_2 distributions. Based on laboratory experiments and image analysis on sixteen greensand samples from the two formations in the Nini field of the North Sea, we found Hermod Formation is only weakly cemented, whereas samples from Ty formation contain cement

545 of berthierine or microcrystalline quartz cement resulting in relatively to lower
546 permeability than Hermod samples.
547
548 We found that the total porosity measured by Archimedes method is to close to Helium
549 porosity, whereas NMR porosity tends to be lower. The discrepancy between Archimedes
550 porosity and NMR porosity may be due to a combination of several factors, including the
551 presence of glauconite grains in greensand.
552
553 This study shows that the surface area measured by BET method and the derived surface
554 relaxivity are associated with the micro-porous glauconite grains. The effective surface
555 area as calculated by Kozeny's equation and as determined from petrographic image
556 analysis of Backscattered Electron Micrographs and the estimated effective surface
557 relaxivity is associated with macro-pores. We found that *Sp* measured by BET method is
558 well correlated with fraction of glauconite plus pore filling clay minerals.
559
560 Irreducible water saturation in the studied greensands ranges from 22% to 41% and these
561 high values are due to the high specific surface area of glauconite. The micro-pores of
562 glauconite remain brine filled even at a capillary pressure of 100 psi.
563
564 We found that predicted permeability from NMR by using Kozeny's equation agrees well
565 when surface relaxivity is known. By using Timur-Coates model, predicting permeability
566 works rather well if we optimize the constant to C=8.3.
567

568 This study shows that predicted capillary pressure curves from NMR T_2 distribution
569 overlay on measured capillary pressure curves for low permeability samples. The
570 deviation between the P_c NMR and P_c lab for the high permeability samples is due to the
571 contrasting relaxivity on the surface of quartz and glauconite.
572

Acknowledgements

Niels Springer and Hans Jørgen Lorentzen (GEUS, DK) are thanked for help with the core analysis. Sinh Hy Nguyen (DTU, DK) performed XRD and BET measurements, Hector Ampuero Diaz (DTU, DK) prepared polished thin sections. DONG Energy A/S is acknowledged for financial support.

Appendix

Nomenclature

BFV	Bound fluid volume
C	Formation dependent constant
c	Kozeny factor
f_i	Amplitude of each T_{2i}
FFI	Free fluid volume
k	Klinkenberg permeability,
K	Scaling factor
S	Specific surface area of bulk
S_g	Specific surface area of grains
Sp	Specific surface of pores
T_{2Bulk}	Relaxation of fluids
$T_{2Diffisionk}$	Relaxation of molecular diffusion
$T_{2Surface}$	Relaxation of surface

595

596 **Greek symbols**

597 ϕ Porosity (fraction)

598 ρ Surface relaxivity

599 τ Inter echo spacing.

600

601 **Unit conversion**

602

603 1 mD = 0.9869 10^{-15} m^2

604 1 psi = 6.89 kPa

605

606 ## References

607

608 Al-Mahrooqi, S. H., Grattoni, C. A., Muggeridge, A. H., Zimmerman, R. W. & Jing, X.
609 D. 2006. Pore-scale modeling of NMR relaxation for the characterization of wettability.
610 *Journal of Petroleum Science and Engineering*, **52**, 172-186.

611 Al-Mahrooqi, S. H., Grattoni, C. A., Moss, A. K. & Jing, X. D. 2003. An investigation of
612 the effect of wettability on NMR characteristics of sandstone rock and fluid systems.
613 *Journal of Petroleum Science and Engineering*, **39**, 389-398.

614 Borre, M., Lind, I. & Mortensen, J. 1997. Specific surface as a measure of burial
615 diagenesis of chalk. *Zentralblatt fur Geologie und Palaontologie*, **1**, 1071–1078.

616 Cagatay, M. N., Saner, S., Al-Saiyed, I. & Carrigan, W. J. 1996. Diagenesis of the
617 Safaniya Sandstone Member (mid-Cretaceous) in Saudi Arabia. *Sedimentary Geology*,
618 **105**, 221-239.

619 Coates, G. R., Xiao, L., et al. 1999. *NMR logging principles and applications*. Gulf
620 Professional Publishing, Houston, Texas, 234.

621 Diaz, E., Prasad, M., Mavko, G. & Dvorkin, J. 2003. Effect of glauconite on the elastic
622 properties, porosity, and permeability of reservoir rocks. *The Leading Edge*, **22**, 42-45.

623 Dodge, W. S., Shafer, J. L., Guzman-Garcia, A. G., & Noble, D. A. 1995. Core and Log
624 NMR Measurements of an Iron-Rich, Glauconitic Sandstone Reservoir. *36th Annual*
625 *Symposium of SPWLA*, Paris, France, June 26-29.

626 Glover, P., Zadjali, I. & Frew, K. 2006. Permeability prediction from MICP and NMR
627 data using an electrokinetic approach. *Geophysics*, **71**, 49-60.

628 Grattoni, C. A., Al-Mahrooqi, S. H., Moss, A. K., Muggeridge, A. H. & Jing, X. D. 2003.
629 An improved technique for deriving drainage capillary pressure from NMR T_2
630 distributions. *The International Symposium of the Society of Core Analysis,* **25,** 21-24
631 September, Pau, France.

632 Hamada, G., Al-Blehed, M., Al-Awad, M. & Al-Saddique, M. 2001. Petrophysical
633 evaluation of low-resistivity sandstone reservoirs with nuclear magnetic resonance log.
634 *Journal of Petroleum Science and Engineering,* **29**, 129-138.

635 Hidajat, I., Singh, M., Cooper, J. & Mohanty, K. K. 2002. Permeability of porous media
636 from simulated NMR response. *Transport in Porous Media,* **48**, 225-247.

637 Hocking, R., Voon, J. & Collins, L. 1988. Stratigraphy and sedimentology of the basal
638 Winning Group, northern Carnarvon Basin. In: P.G. Purcell and R.R. Purcell (editors),
639 The North West Shelf, Proceedings of Petroleum Exploration Society Australia
640 Symposium, Perth, 203–224.

641 Hossain, Z., Fabricius, I. L. & Christensen, H. F. 2009. Elastic and nonelastic
642 deformation of greensand. *The Leading Edge,* **28**, 260-262.

643 Howard, J. J., Kenyon, W. E. & Straley, C. 1993. Proton magnetic resonance and pore
644 size variations in reservoir sandstones. *SPE Formation Evaluation,* **1**, 194-200.

645 Kenyon, B., Kleinberg, R., Straley, C. & Morriss, C. 1995. Nuclear Magnetic Resonance
646 Imaging—Technology for the 21st Century. *Oilfield Review,* **7**, 19–30.

647 Kenyon, W. E. 1997. Petrophysical principles of applications of NMR logging. *The Log*
648 *Analyst,* **38**, 21-43.

649 Kewan, W. & Ning, L. 2008. Numerical simulation of rock pore-throat structure effects
650 on NMR T2 distribution. *Applied Geophysics,* **5**, 86-91.

651 Kleinberg, R. 1996. Utility of NMR T_2 distributions, connection with capillary pressure,
652 clay effect, and determination of the surface relaxivity parameter ρ_2. *Magnetic resonance*
653 *imaging*, **14**, 761-767.

654 Kozeny, J. 1927. Ueber kapillare Leitung des Wassers im Boden.
655 *Sitzungsber.Akad.Wiss.Wien,* **136**, 271-306.

656 Marschall, D., Gardner, J. S., Mardon, D. & Coates, G. R. 1995. Method for correlating
657 NMR relaxometry and mercury injection data. *Proceeding of the 1995 International*
658 *Symposium of Society of core Analysts*, papers 9511.

659 Mortensen, J., Engstrøm, F. & Lind, I. 1998. The relation among porosity, permeability,
660 and specific surface of chalk from the Gorm field, Danish North Sea. *SPE Reservoir*
661 *Evaluation and Engineering,* **1**, 245-251.

662 Ranganathan, V. & Tye, R. S. 1986. Petrography, diagenesis, and facies controls on
663 porosity in Shannon Sandstone, Hartzog Draw Field, Wyoming. *AAPG Bulletin*, **70**, 56-
664 69.

665 Riepe, L. 1998. Specific internal surface: the “forgotten?” petrophysical measurement!
666 *Proceeding of the 1998 International Symposium of Society of core Analysts,* papers
667 9540.

668 Rueslåtten, H., Eidesmo, T., Lehne, K. A. & Relling, O. M. 1998. The use of NMR
669 spectroscopy to validate NMR logs from deeply buried reservoir sandstones. *Journal of*
670 *Petroleum Science and Engineering*, **19**, 33-44.

671 Rueslåtten, H., Eidsemo, T. & Slot-Petersen, C. 1998. NMR studies of iron-rich
672 sandstone oil reservoir. *Proceeding of the 1998 International Symposium of Society of*
673 *core Analysts,* papers 9821

674 Schiøler, P., Andsbjerg, J., Clausen, O. R., Dam, G., Dybkjær, K., Hamberg, L.,
675 Heilmann-Clausen, C., Johannessen, E. P., Kristensen, L. E. and Prince, I., 2007.
676 *Lithostratigraphy of the Paleocene: Lower Neogene succession of the Danish North Sea*.
677 Geological Survey of Denmark and Greenland, Danish Ministry of the Environment
678 report 77.

679 Slot-Petersen, C., Eidsemo, T., White, J. & Rueslatten, H. G. 1998. NMR formation
680 evaluation application in a complex low resistivity hydrocarbon reservoir. *Transactions*
681 *of the SPWLA 39th Annual Logging Symposium*, Paper 1998-TT

682 Solymar, M. & Fabricius, I. L. 1999. Image analysis and estimation of porosity and
683 permeability of Arnager Greensand, Upper Cretaceous, Denmark. *Physics and Chemistry*
684 *of the Earth Part A-Solid Earth and Geodesy, **24***, 587-591.

685 Solymar, M., Fabricius, I. L. & Middleton, M. 2003. Flow characterization of glauconitic
686 sandstones by integrated Dynamic Neutron Radiography and image analysis of
687 backscattered electron micrographs. *Petroleum Geoscience,* **9**, 175-183.

688 Stokkendal, J., Friis, H., Svendsen, J. B., Poulsen, M. L. K. & Hamberg, L. 2009.
689 Predictive permeability variations in a Hermod sand reservoir, Stine Segments, Siri Field,
690 Danish North Sea. *Marine and Petroleum Geology*, **26**, 397-415.

691 Straley, C., Roosini, D., Vinegar, H., Tutunjian, P. & Morriss, C. 1997. Core analysis by
692 low-field NMR. *The Log Analyst,* **38**, 84-94.

693 Tilley, B. J. & Longstaffe, F. J. 1984. Controls on hydrocarbon accumulation in
694 glauconitic sandstone, Suffield heavy oil sands, southern Alberta. *AAPG Bulletin,* **68**,
695 1004-1023.

696 Underwood, E. E. 1970. *Quantitative stereology*. Addison -Wesley, Reading,
697 Massachusetts, 270.

698 Volokitin, Y., Looyestijn, W. J., Slijkerman, W. F. J. & Hofman, J. P. 1999. A Practical
699 Approach to Obtain 1st Drainage Capillary Pressure Curves From NMR Core and Log
700 Data. *The International Symposium of the Society of Core Analysts,* **24**, 1–4.

701 Winn, R. D. 1994. Shelf Sheet-Sand Reservoir of the Lower Cretaceous Greensand,
702 North Celtic Sea Basin, Offshore Ireland. *AAPG Bulletin*, **78**, 1775-1789.

703 Xie, R. H., Xiao, L. Z., Wang, Z. D. & Dunn, K. J. 2008. The influence factors of NMR
704 logging porosity in complex fluid reservoir. *Science in China Series D: Earth Sciences*,
705 **51**, 212-217.

706

Figure captions

Fig. 1. BSE images of greensand samples. (a) Sample 1-4 from Hermod Formation and (b) sample 1A-142 from Ty Formation. Scale bar is 200 µm. Q: quartz; Gl: glauconite; H: Heavy minerals, M: Mica; PF: pore filling clay minerals. Porosity, permeability and irreducible water saturation are 37 p.u., 530 mD and 26% for sample 1-4 and 29 p.u., 150 mD and 38% for sample 1A-142.

Fig. 2. Location map showing the position of the Nini-1 well used in this study (arrow). The margins of the Siri Canyon are shown by grey shading. An area of positive relief within the canyon is also shown by grey shading. G, Germany; N, Norway; NL, Netherlands; S, Sweden; UK, United Kingdom (Figure modified after Schiøler *et al.* 2007).

Fig. 3. Gamma ray, porosity and resistivity logs for wells Nini-1 (top) and Nini-1A (bottom). The glauconite bearing reservoir intervals (Hermod sand and Ty sand) have relatively low separation between neutron- and density porosity. Horizontal dashed lines indicate the studied core intervals. Core data are shown for reference. Permeability is higher in Hermod sand than in Ty sand.

Fig. 4: Macro-porosity and micro-porosity determination for sample 1-4 (a) from NMR T_2 distribution (b) from the capillary pressure curve. The cumulative distribution for the fully saturated sample is compared to the cumulative distribution after centrifuging at 100

730 psi. The cutoff time which separates the T_2 distribution into macro-porosity and micro-
731 porosity is defined as the relaxation time at the point where the cumulative porosity of the
732 fully saturated sample equals the irreducible water saturation. The dashed vertical line is
733 shown a cutoff of 5.21 ms. The capillary pressure of 100 psi corresponds to a micro-
734 porosity of 9.1%.
735
736 **Fig. 5.** Cross plot of macro-porosity from capillary pressure measurement and
737 permeability. Samples from the Hermod sand have similar porosity and permeability,
738 whereas the samples from Ty sand are more scattered. The reference lines represent equal
739 specific surface of pores (*Sp (Kozeny)*) in μm^{-1} as calculated by using Kozeny's equation.
740 The data indicate that *Sp* is lower in Hermod sand than in Ty sand.
741
742 **Fig. 6.** Bulk composition of investigated samples from Hermod and Ty Formations of the
743 Nini Field. Mineral composition was determined by point counting of 500 points across
744 each entire thin-section. Macro-porosity was determined by image analysis when porosity
745 threshold is equal to macro-porosity determined from P_c measurements. Micro-porosity is
746 the difference between Helium porosity and image porosity.
747
748 **Fig. 7.** (a), (c) Capillary pressure curves and (b), (d) NMR T_2 distribution curves of
749 greensand samples. (a) P_c curves of Hermod Formation samples are shifted toward low
750 irreducible water saturation, whereas (c) the Ty Formation samples have relatively high
751 irreducible water saturation. This pattern compares to the relatively high permeability of
752 Hermod sand relative to the low permeability of Ty sand (Fig. 3). T_2 distribution of all

753 samples shows two peaks. The peak close to 1 ms represents micro-porosity and the peak
754 close to 100 ms represents macro-porosity.
755
756 **Fig. 8.** (a) Helium porosity, Archimedes porosity and NMR porosity of investigated
757 samples. Helium porosity tends to be the highest, whereas NMR porosity is
758 underestimated due to iron bearing minerals in greensand. (b) Cross plot of delta porosity
759 (Archimedes porosity-NMR porosity) and minerals bulk composition (glauconite, pore
760 filling clay and clay coating). Cross plots of (c) macro-porosity and (d) micro-porosity
761 from NMR T_2 distribution and capillary pressure curves.
762
763 **Fig. 9.** Correlation between specific surface of pores as measured by BET (*Sp (BET)*) and
764 (a) irreducible water saturation as determined from NMR measurements, (b) irreducible
765 water saturation as determined from capillary pressure measure as well as (c) clay
766 minerals (glauconite, clay coating and pore filling clay) as percentage of bulk
767 composition.
768
769 **Fig. 10.** (a) Specific surface area with respect to pore (*Sp*) determined by BET nitrogen
770 adsorption (*Sp (BET)*), estimated from Kozeny's equation (*Sp (Kozeny)*) and determined
771 by image analysis of the BSE images (*Sp (image)*). (b) Surface relaxivity determined
772 comparing T_2 distribution with *Sp (BET)*, *Sp (Kozeny)*, and *Sp (image)*. For two samples,
773 surface relaxivity are also determined from capillary pressure versus NMR T_2
774 distribution.
775

776 **Fig. 11.** (a), (b) Porosity distribution and cumulative porosity for five greensand samples.
777 (c), (d) Permeability distribution of five greensand samples obtained from Kozeny's
778 equation.
779
780 **Fig. 12.** Measured permeability versus NMR predicted permeability by using surface
781 relaxivity from (a) *Sp(Kozeny)*, (b) *Sp(image)*, (c) *Sp(BET)*, (d) P_c versus NMR and (e)
782 from Timur-Coates model. (g) Measured permeability versus predicted permeability from
783 image analysis. Image permeability and NMR predicted permeability by using surface
784 relaxivity from *Sp(image)* are equal.
785
786 **Fig. 13.** Air Brine capillary pressure curves including saturation error compared with
787 NMR derived capillary pressure including saturation error. Saturation error corresponds
788 to the error associated with porosity measurements. The NMR derived capillary pressure
789 curves are based on surface relaxivity value of 20.4 μm/s for Hermod Formation and 28.4
790 μm/s for Ty formation. Deviation between average surface relaxivity (solid line) and
791 surface relaxivity for predicting P_c NMR (dashes line) are shown (e) for Hermod
792 Formation and (f) for Ty Formation.
793

List of tables

Table 1. *Core plug porosity data. Helium porosity was measured by Helium gas expansion, Archimedes porosity was measured by immersing, and NMR porosity was measured by the signal amplitude of T_2 measurements respectively. Archimedes macro-porosity and NMR macro-porosity were determined from capillary pressure curves and T_2 distributions respectively.*

Table 2. *Core plug data. Specific surface area of grains (SSA) was measured by BET method and effective specific surface of pores (Sp(Kozeny)) was calculated by using Kozeny's equation. Image specific perimeter of pores (Sp(image)) was determined by image analysis by using the method of Borre et al. (1997). The cutoff time which separates the T_2 distribution into macro-porosity and micro-porosity is defined as the relaxation time at the point where the cumulative porosity of the fully saturated sample equals the irreducible water saturation.*

Fig. 1

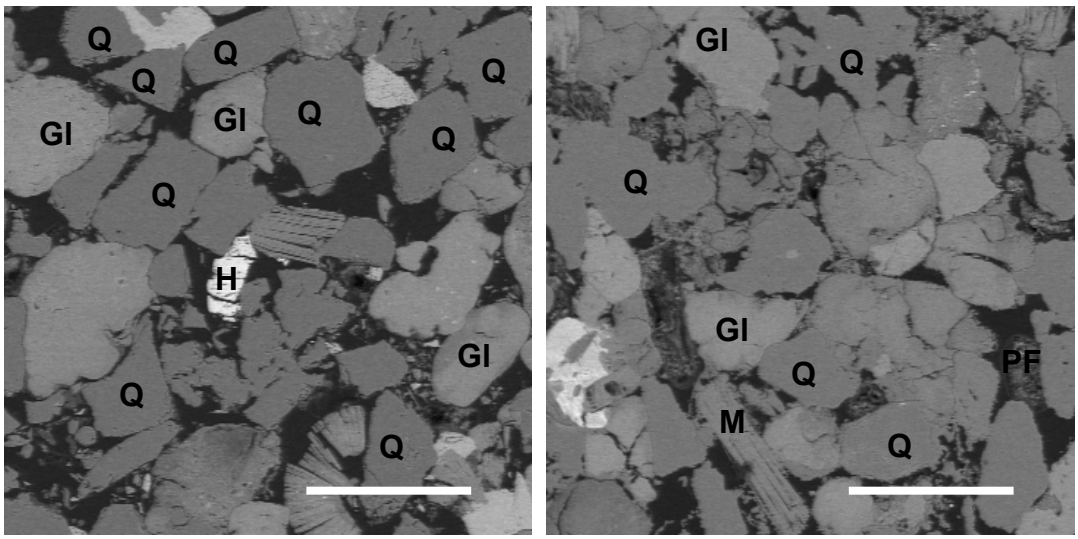

(a) (b)

Fig. 2

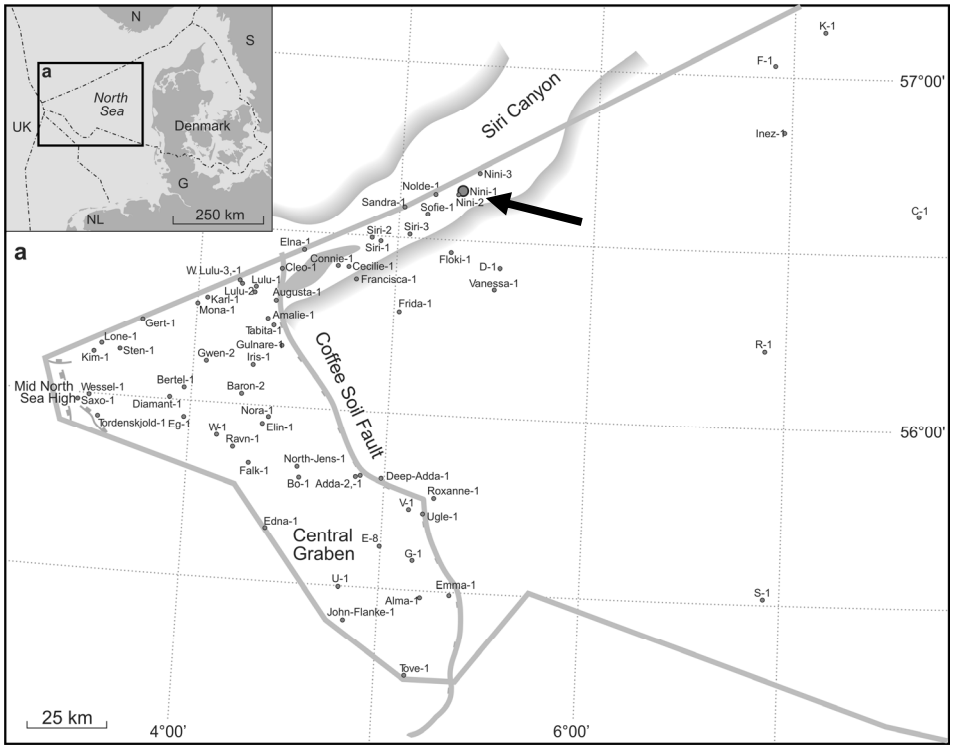
N
S
a
North Sea
UK
Denmark
G
NL
250 km
a
Siri Canyon
Nolde-1
Nini-3
Nini-1
Nini-2
Sandra-1
Sofie-1
Siri-2
Siri-3
Siri-1
Elna-1
Connie-1
Cleo-1
Cecilie-1
Floki-1
D-1
W.Lulu-3,-1
Lulu-1
Lulu-2
Francisca-1
Vanessa-1
Augusta-1
Karl-1
Mona-1
Frida-1
Amalie-1
Gert-1
Tabita-1
Lone-1
Sten-1
Kim-1
Gulnare-1
Gwen-2
Iris-1
Coffee Soil Fault
Mid North Sea High
Wessel-1
Saxo-1
Bertel-1
Baron-2
Diamant-1
Nora-1
Tordenskjold-1
Fg-1
W-1
Elin-1
Ravn-1
Falk-1
North-Jens-1
Bo-1
Adda-2,-1
Deep-Adda-1
Roxanne-1
V-1
Ugle-1
Edna-1
Central Graben
E-8
G-1
U-1
Emma-1
Alma-1
John-Flanke-1
Tove-1
K-1
F-1
Inez-1
C-1
R-1
S-1
57°00'
56°00'
4°00'
6°00'
25 km

Fig. 3

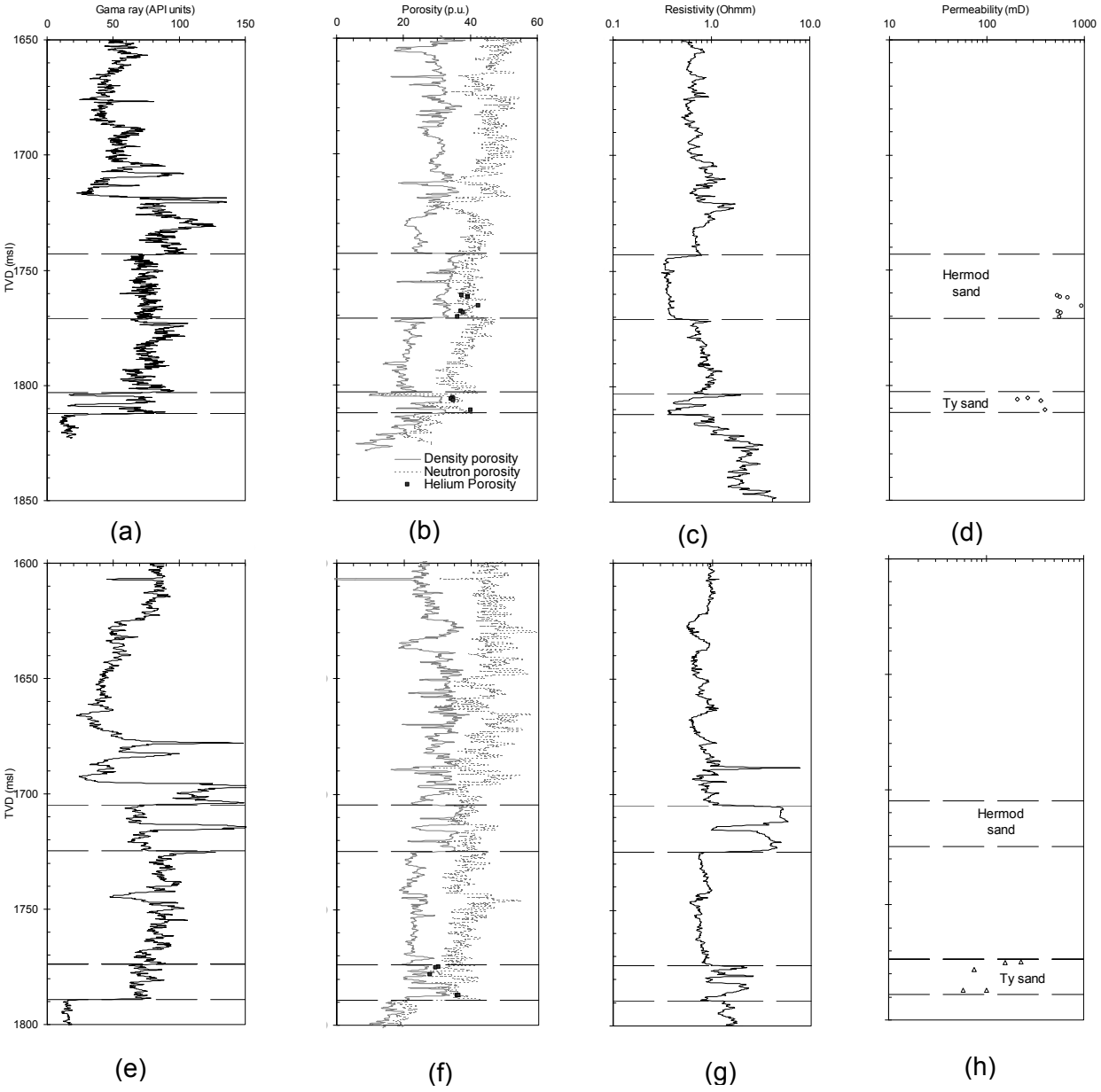
Gama ray (API units)
0
50
100
150
Porosity (p.u.)
0
20
40
60
Resistivity (Ohmm)
0.1
1.0
10.0
Permeability (mD)
10
100
1000
TVD (msl)
1650
1700
1750
1800
1850
Hermod sand
Ty sand
Density porosity
Neutron porosity
Helium Porosity
(a)
(b)
(c)
(d)
1600
1650
1700
1750
1800
Hermod sand
Ty sand
(e)
(f)
(g)
(h)

Fig. 4

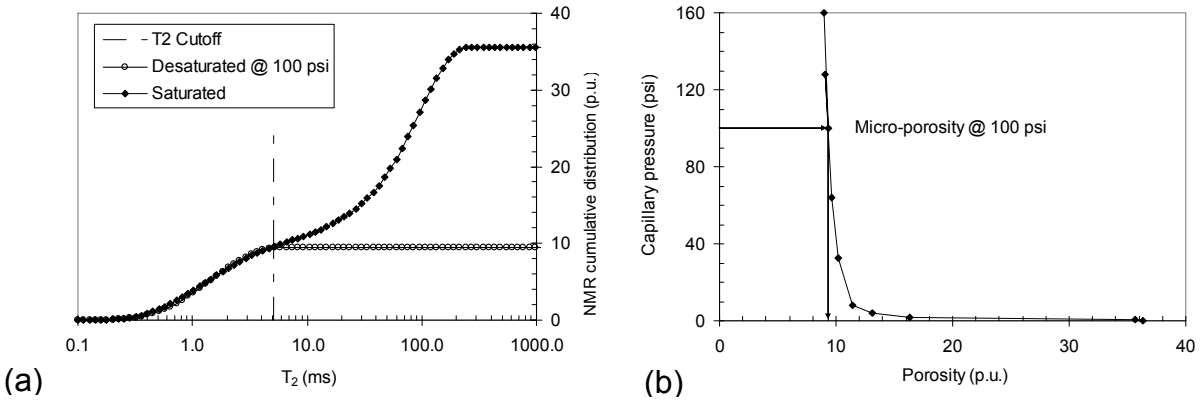
T2 Cutoff
Desaturated @ 100 psi
Saturated
NMR cumulative distribution (p.u.)
0
10
20
30
40
0.1
1.0
10.0
100.0
1000.0
T2 (ms)
(a)
Capillary pressure (psi)
0
40
80
120
160
Micro-porosity @ 100 psi
0
10
20
30
40
Porosity (p.u.)
(b)

Fig. 5

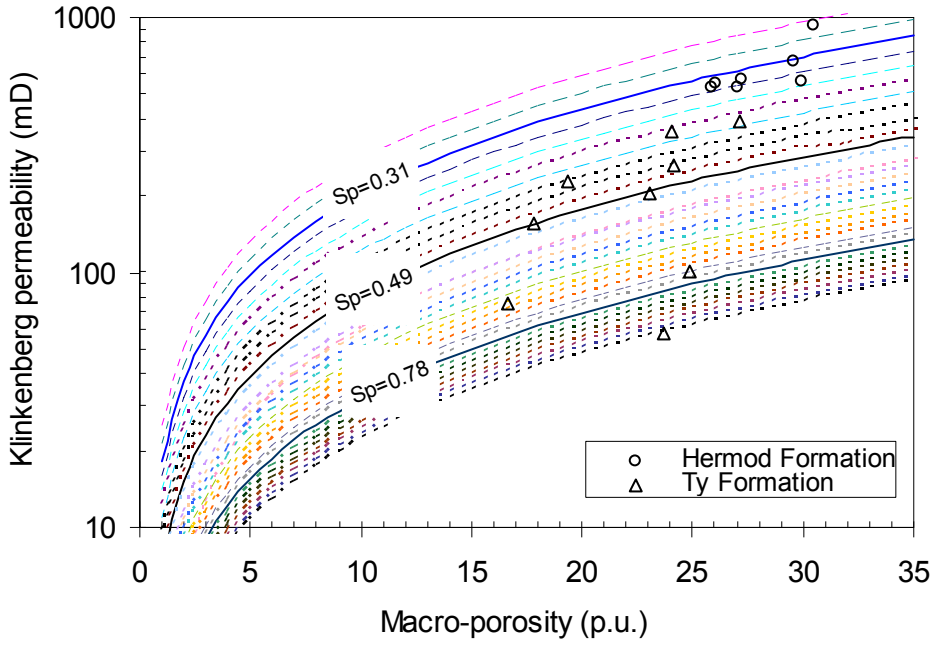
1000
100
10
Klinkenberg permeability (mD)
0
5
10
15
20
25
30
35
Macro-porosity (p.u.)
Sp=0.31
Sp=0.49
Sp=0.78
Hermod Formation
Ty Formation

Fig. 6

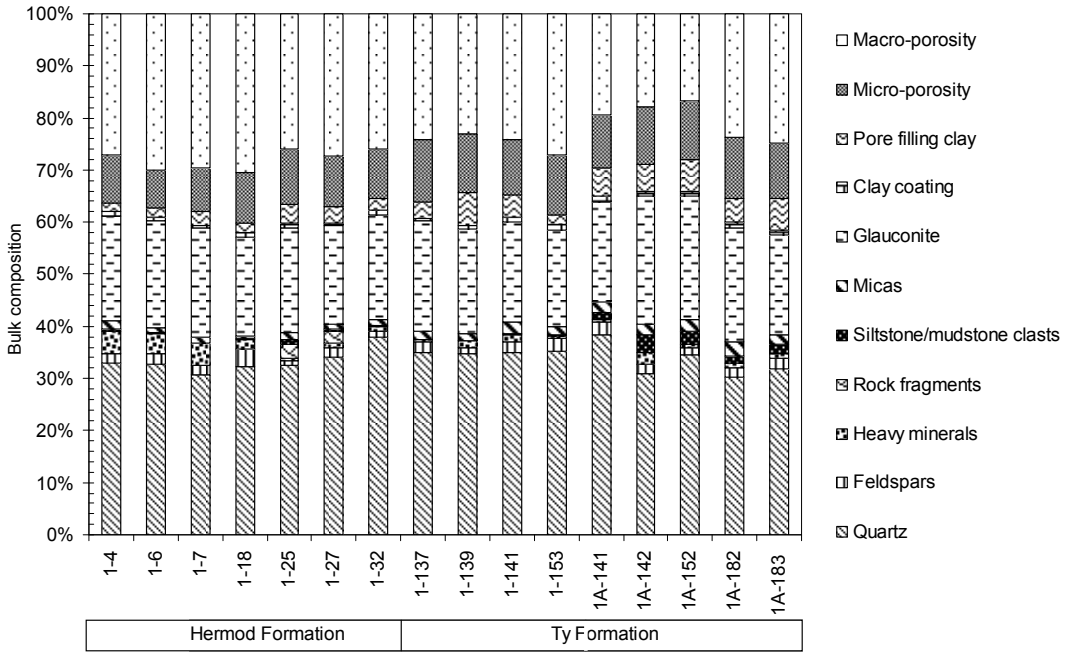
100%
90%
80%
70%
60%
50%
40%
30%
20%
10%
0%
Bulk composition
1-4
1-6
1-7
1-18
1-25
1-27
1-32
1-137
1-139
1-141
1-153
1A-141
1A-142
1A-152
1A-182
1A-183
Hermod Formation
Ty Formation
Macro-porosity
Micro-porosity
Pore filling clay
Clay coating
Glauconite
Micas
Siltstone/mudstone clasts
Rock fragments
Heavy minerals
Feldspars
Quartz

Fig. 7

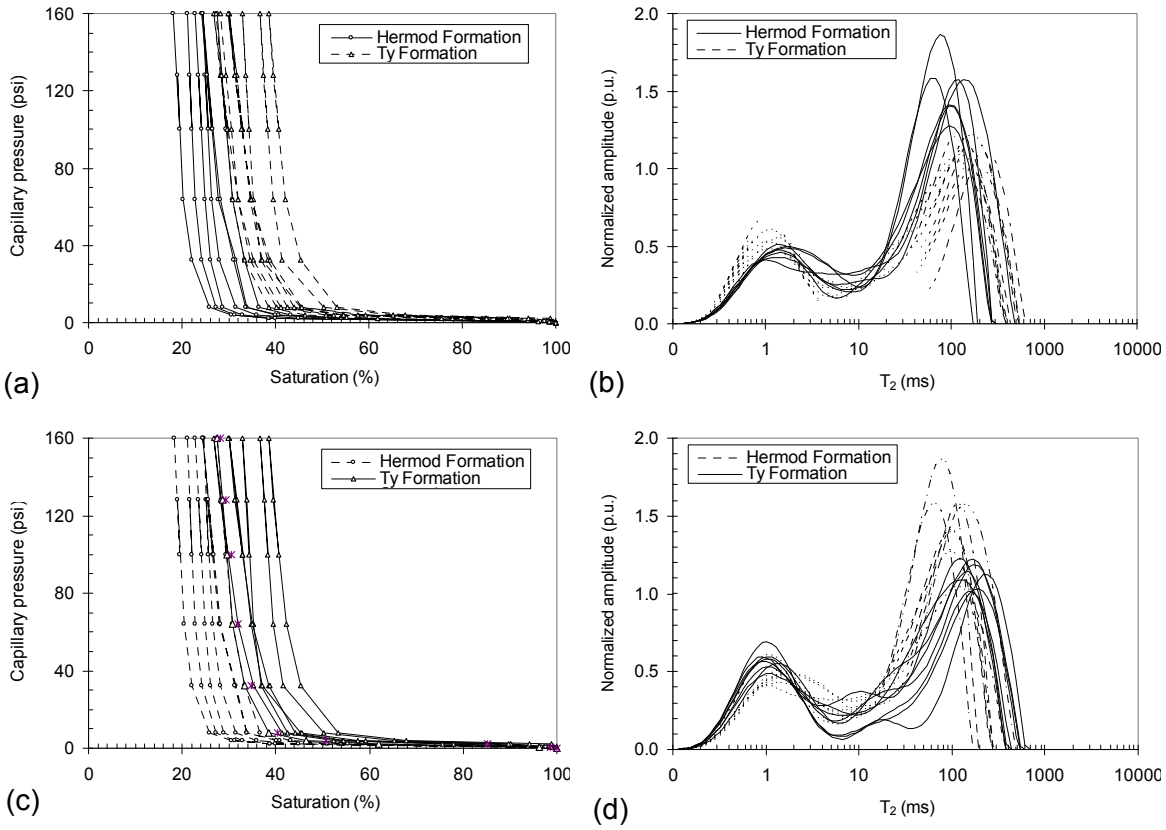
Hermod Formation
Ty Formation
Capillary pressure (psi)
Saturation (%)
(a)
Normalized amplitude (p.u.)
T_2 (ms)
(b)
(c)
(d)

Fig. 8

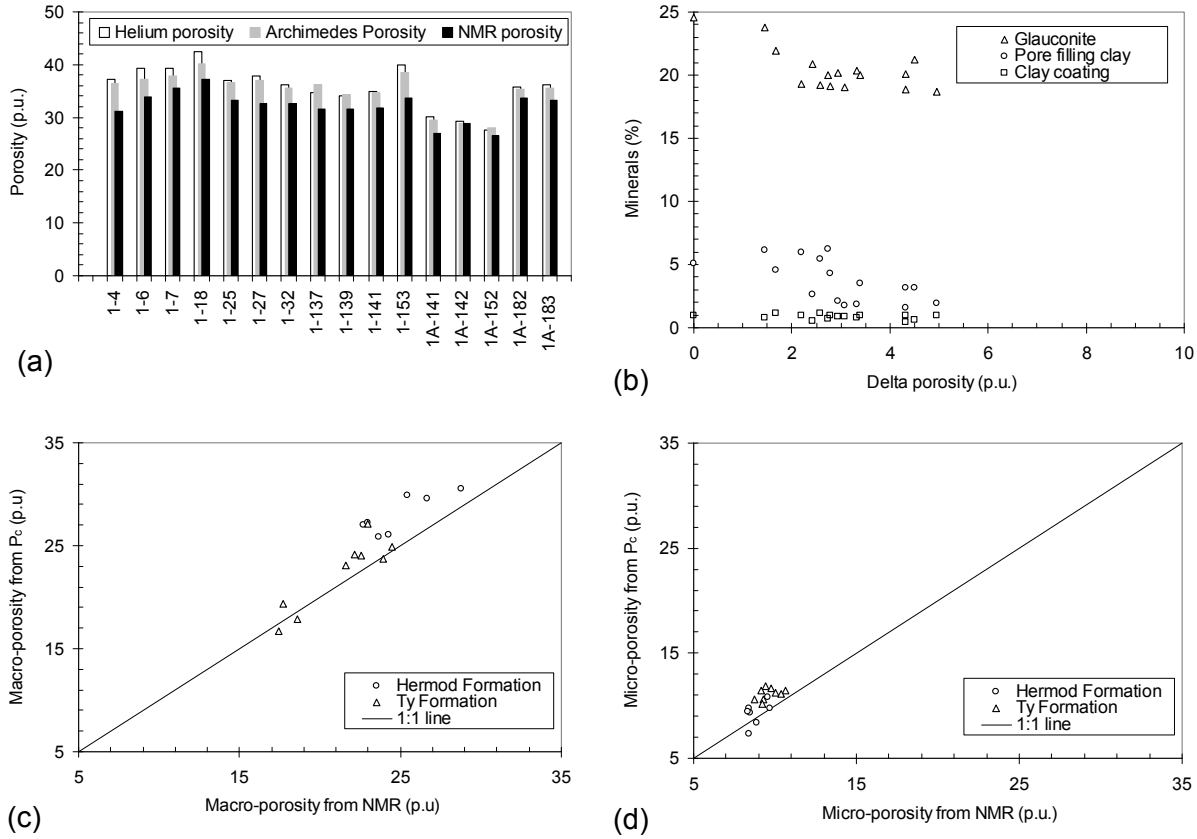
Helium porosity
Archimedes Porosity
NMR porosity
Porosity (p.u.)
1-4
1-6
1-7
1-18
1-25
1-27
1-32
1-137
1-139
1-141
1-153
1A-141
1A-142
1A-152
1A-182
1A-183
(a)
Glauconite
Pore filling clay
Clay coating
Minerals (%)
Delta porosity (p.u.)
(b)
Hermod Formation
Ty Formation
1:1 line
Macro-porosity from Pc (p.u)
Macro-porosity from NMR (p.u)
(c)
Micro-porosity from Pc (p.u.)
Micro-porosity from NMR (p.u.)
(d)

Fig. 9

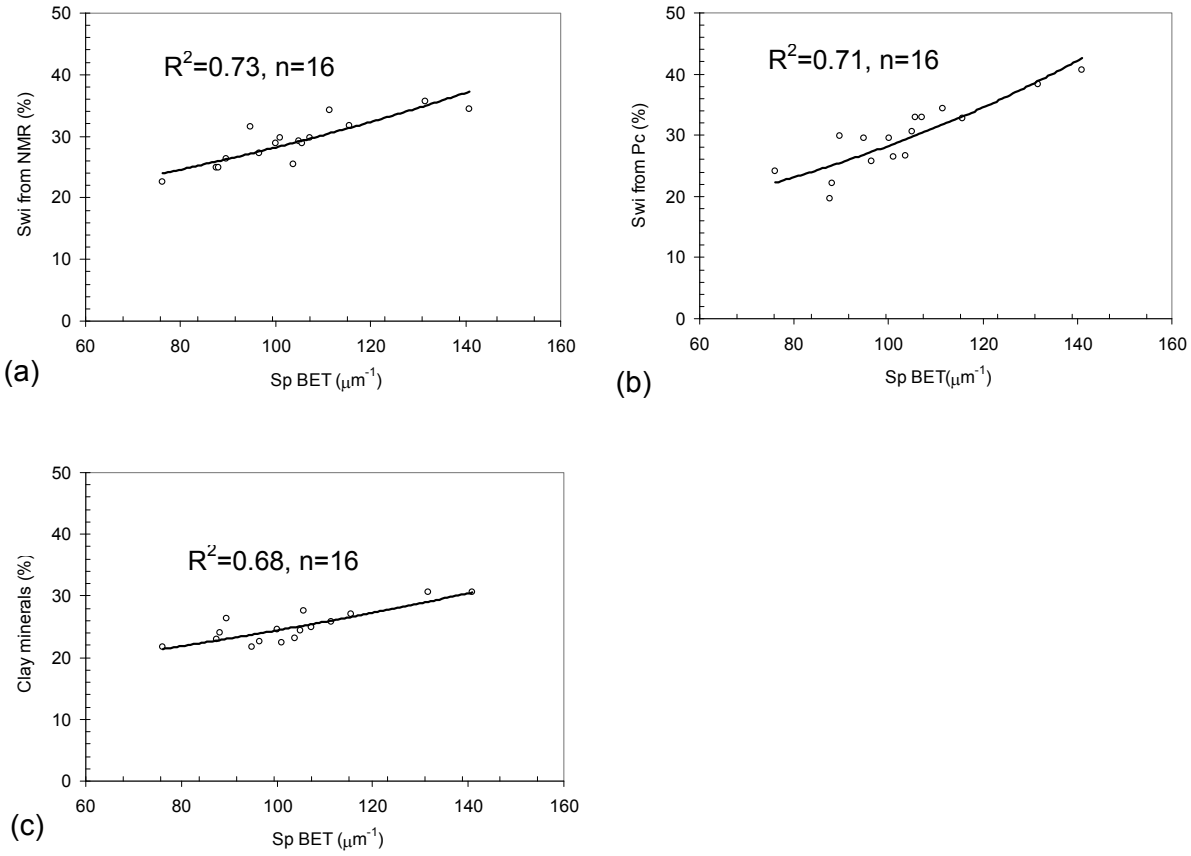
R2=0.73, n=16
Swi from NMR (%)
Sp BET (μm-1)
(a)
R2=0.71, n=16
Swi from Pc (%)
Sp BET(μm-1)
(b)
R2=0.68, n=16
Clay minerals (%)
Sp BET (μm-1)
(c)

Fig. 10

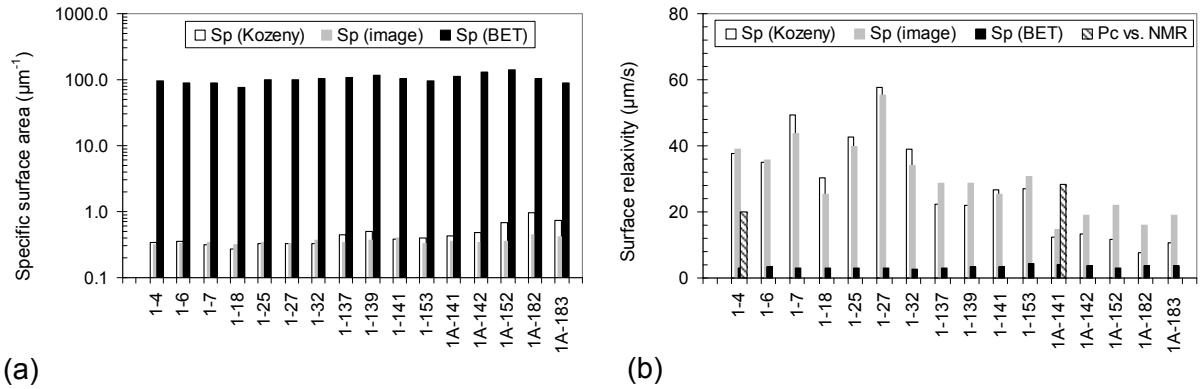
Specific surface area (μm-1)
1000.0
100.0
10.0
1.0
0.1
Sp (Kozeny)
Sp (image)
Sp (BET)
1-4
1-6
1-7
1-18
1-25
1-27
1-32
1-137
1-139
1-141
1-153
1A-141
1A-142
1A-152
1A-182
1A-183
(a)
Surface relaxivity (μm/s)
80
60
40
20
0
Sp (Kozeny)
Sp (image)
Sp (BET)
Pc vs. NMR
1-4
1-6
1-7
1-18
1-25
1-27
1-32
1-137
1-139
1-141
1-153
1A-141
1A-142
1A-152
1A-182
1A-183
(b)

Fig. 11

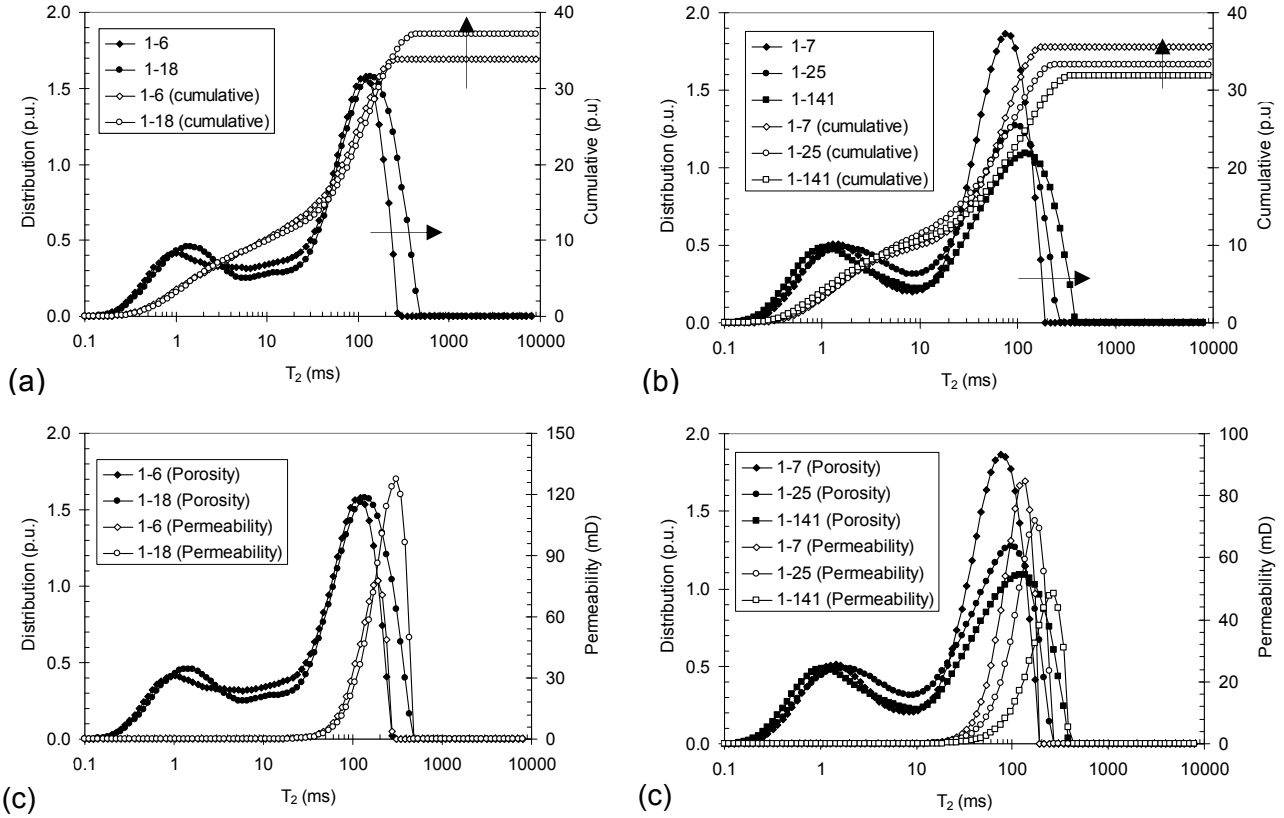
1-6
1-18
1-6 (cumulative)
1-18 (cumulative)
Distribution (p.u.)
Cumulative (p.u)
T2 (ms)
(a)
1-7
1-25
1-141
1-7 (cumulative)
1-25 (cumulative)
1-141 (cumulative)
Distribution (p.u.)
Cumulative (p.u)
T2 (ms)
(b)
1-6 (Porosity)
1-18 (Porosity)
1-6 (Permeability)
1-18 (Permeability)
Distribution (p.u.)
Permeability (mD)
T2 (ms)
(c)
1-7 (Porosity)
1-25 (Porosity)
1-141 (Porosity)
1-7 (Permeability)
1-25 (Permeability)
1-141 (Permeability)
Distribution (p.u.)
Permeability (mD)
T2 (ms)
(c)

Fig. 12

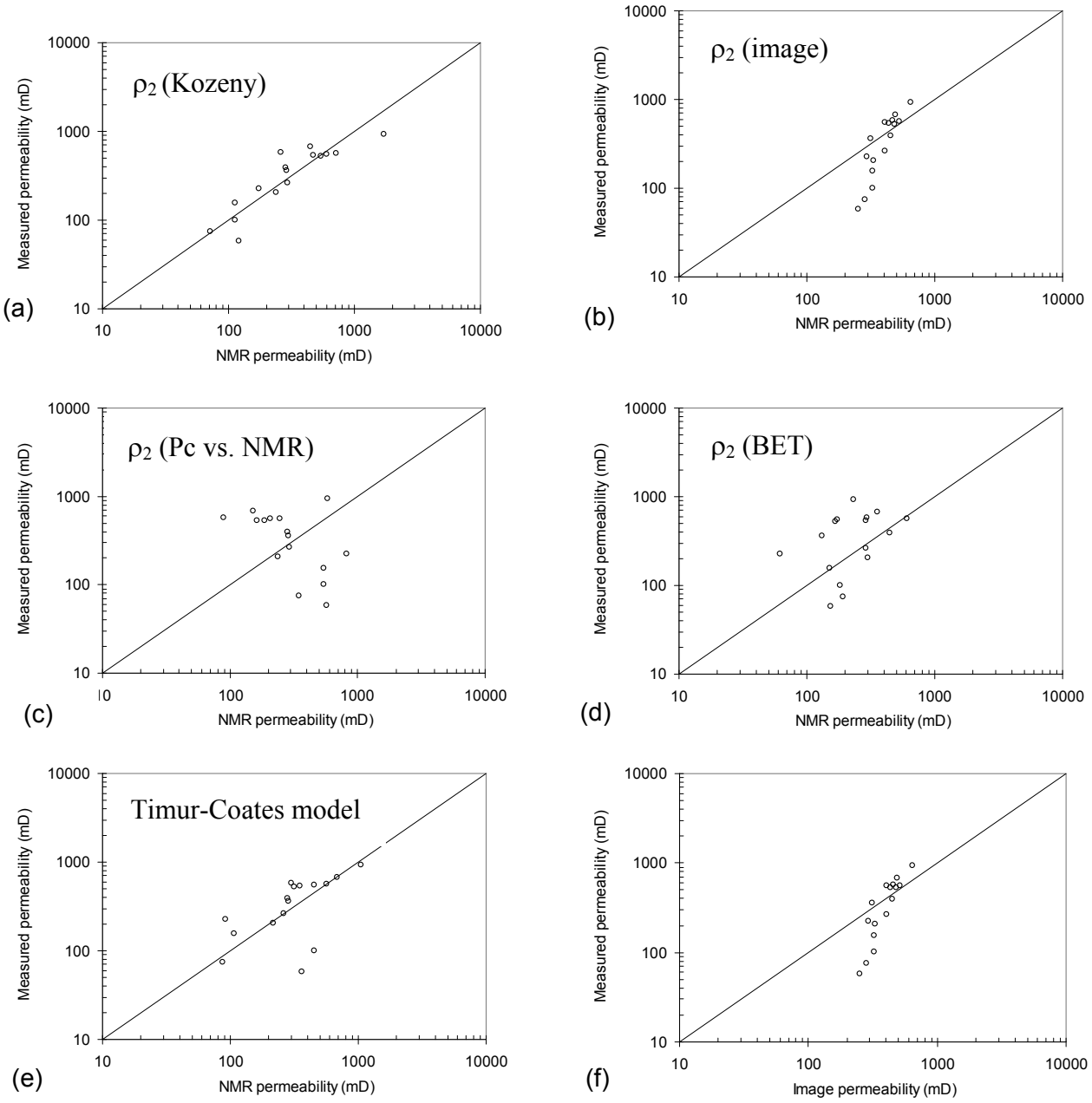
ρ2 (Kozeny)
Measured permeability (mD)
NMR permeability (mD)
(a)
ρ2 (image)
Measured permeability (mD)
NMR permeability (mD)
(b)
ρ2 (Pc vs. NMR)
Measured permeability (mD)
NMR permeability (mD)
(c)
ρ2 (BET)
Measured permeability (mD)
NMR permeability (mD)
(d)
Timur-Coates model
Measured permeability (mD)
NMR permeability (mD)
(e)
Measured permeability (mD)
Image permeability (mD)
(f)
10
100
1000
10000

Fig. 13

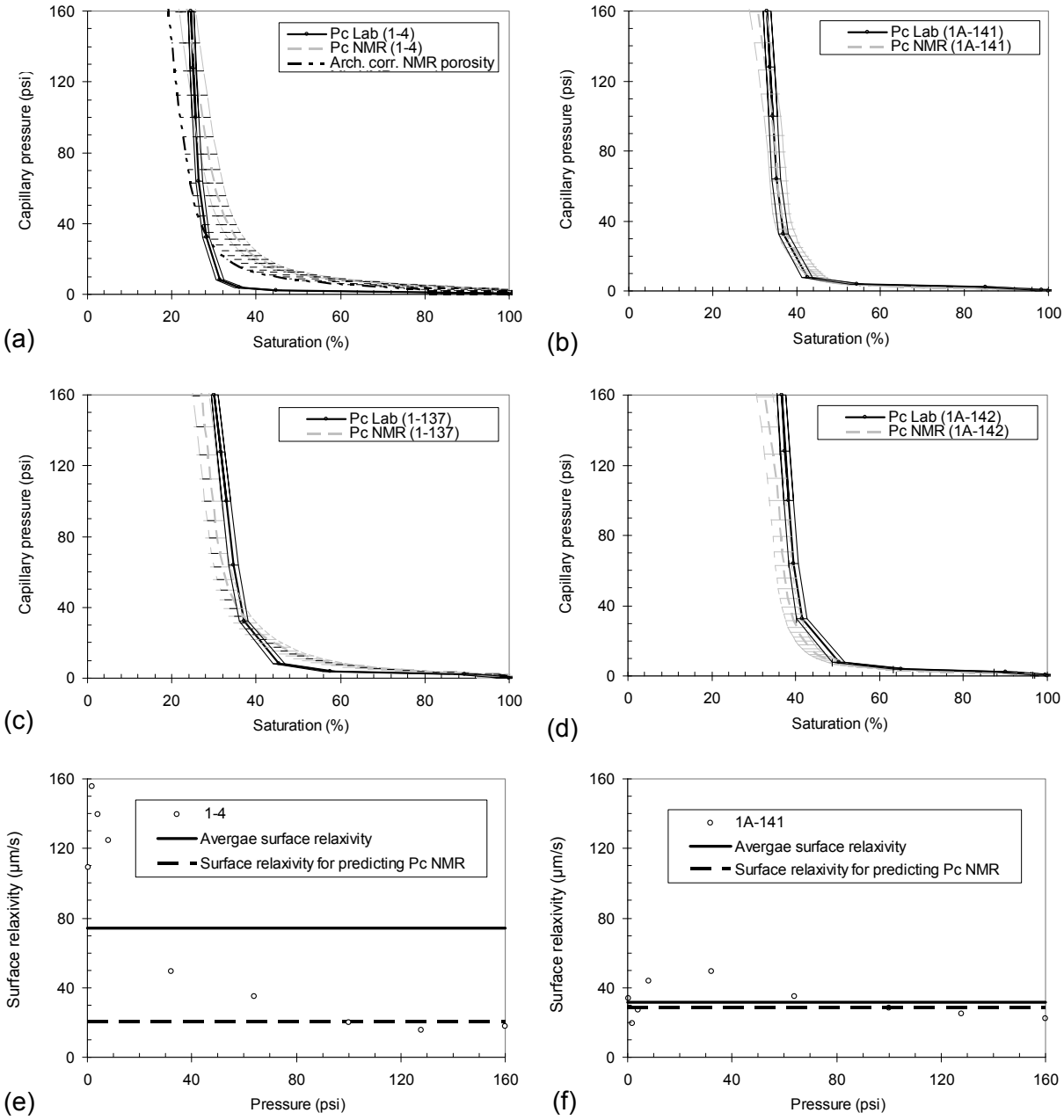
Pc Lab (1-4)
Pc NMR (1-4)
Arch. corr. NMR porosity
Capillary pressure (psi)
Saturation (%)
(a)
Pc Lab (1A-141)
Pc NMR (1A-141)
Capillary pressure (psi)
Saturation (%)
(b)
Pc Lab (1-137)
Pc NMR (1-137)
Capillary pressure (psi)
Saturation (%)
(c)
Pc Lab (1A-142)
Pc NMR (1A-142)
Capillary pressure (psi)
Saturation (%)
(d)
1-4
Avergae surface relaxivity
Surface relaxivity for predicting Pc NMR
Surface relaxivity (µm/s)
Pressure (psi)
(e)
1A-141
Avergae surface relaxivity
Surface relaxivity for predicting Pc NMR
Surface relaxivity (µm/s)
Pressure (psi)
(f)

Table 1

Formation	Measured Depth (m)	TVD (msl)	Sample ID	Helium porosity (p.u.)	Error ±	Archimedes porosity (p.u.)	Error ±	NMR porosity (p.u.)	Error ±	Archimedes macro-porosity (p.u.)	NMR macro-porosity (p.u.)
Hermod	1761.1		1-4	37.3	1.5	35.5	1.1	31.2	0.4	27.0	22.7
	1761.7		1-6	39.3	1.3	37.2	1.1	33.8	0.5	29.9	25.4
	1762.1		1-7	39.2	0.4	37.9	1.1	35.5	0.5	29.6	26.7
	1765.7		1-18	42.4	0.5	40.2	1.2	37.2	0.5	30.5	28.8
	1768.1		1-25	37.1	0.5	36.7	1.1	33.3	0.5	25.9	23.7
	1768.7		1-27	37.8	1.1	37.0	1.1	32.7	0.5	27.2	23.0
	1770.4		1-32	36.2	0.9	35.5	1.1	32.6	0.5	26.0	24.3
Ty	1805.5		1-137	34.7	0.8	36.1	1.1	31.6	0.4	24.2	22.2
	1806.1		1-139	34.2	0.5	34.3	1.0	31.6	0.4	23.1	21.6
	1806.7		1-141	34.9	0.3	34.6	1.0	31.8	0.4	24.1	22.5
	1810.7		1-153	40.0	0.4	38.6	1.2	33.6	0.5	27.2	23.0
	1972.1	1774.7	1A-141	30.1	0.1	29.5	0.9	27.0	0.4	19.4	17.7
	1972.4	1775.0	1A-142	29.3	0.7	29.0	0.9	29.0	0.4	17.9	18.6
	1975.8	1778.1	1A-152	27.7	0.3	28.1	0.8	26.6	0.4	16.7	17.5
	1985.7	1787.0	1A-182	35.7	0.1	35.3	1.1	33.7	0.5	23.7	23.9
	1986.0	1787.2	1A-183	36.2	0.4	35.5	1.1	33.3	0.5	24.9	24.5

Table 2

Sample ID	Klinkenberg permeability (mD)	SSA (BET) (m^2/g)	Sp (Kozeny) (μm^{-1})	Sp (image) (μm^{-1})	T_2 Cutoff (ms)	Irreducible water saturation from P_c (%)	Irreducible water saturation from NMR (%)
1-4	530	21	0.34	0.32	5.2	25.6	27.2
1-6	560	21	0.35	0.33		19.6	24.9
1-7	680	21	0.31	0.35		22.1	24.9
1-18	940	19	0.27	0.32		24.2	22.6
1-25	540	20	0.33	0.35		29.4	28.8
1-27	570	22	0.33	0.33		26.5	29.8
1-32	550	21	0.32	0.36		26.7	25.5
1-137	260	20	0.45	0.34		33.0	29.8
1-139	210	22	0.49	0.38		32.8	31.8
1-141	360	20	0.38	0.39		30.5	29.2
1-153	390	23	0.39	0.33		29.6	31.6
1A-141	230	17	0.43	0.35	3.7	34.4	34.2
1A-142	160	19	0.49	0.35		38.4	35.7
1A-152	80	20	0.68	0.36		40.7	34.4
1A-182	60	22	0.95	0.46		32.9	28.9
1A-183	100	19	0.74	0.41		29.9	26.4